PMM Meeting
Oct 2017
San Diego, CA

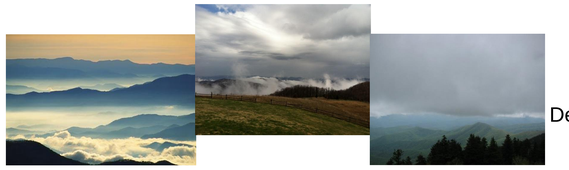

IPHEx Follow-On Studies

Malarvizhi Arulraj, Yajuan (Viola) Duan, Ana P. Barros,

Department of Civil and Environmental Engineering, Pratt School of Engineering, Duke University, NC

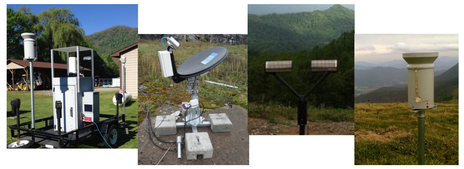

1. Low-level Clouds and Fog in Modifying Orographic Rainfall

A. Seeder-feeder Interactions (SFI) Study using Duke Rain Microphysics Column Model

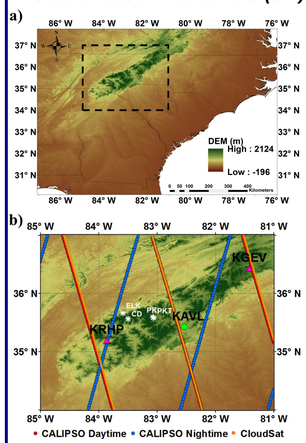

Figure 1 (Left) **–** (**a**) Region of study (in the black box) in context of southeastern United States map; (**b**) Overview of Cloud-Aerosol Lidar and Infrared Pathfinder Satellite Observations (CALIPSO) and CloudSat overpasses over the study region. White asterisks denote the locations of four ground fog collectors at Elkmont (ELK), Clingmans Dome (CD), Purchase Knob (PK), and Purchase Knob Tower (PKT).

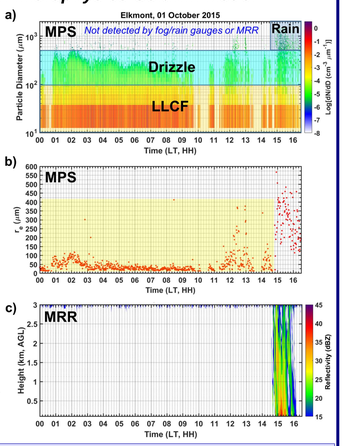

Figure 2 (Right) **–** Time series of drop size distributions (**a**) from the meteorological particle spectrometer (MPS), droplet effective radius (r_e; **b**) derived from the MPS spectra, and reflectivity profiles (**c**) from a collocated Micro Rain Radar (MRR) at Elkmont on 1 October 2015. Note the shaded area in (**b**) highlights the fog presence.

To probe SFI between fog and incoming precipitating systems, **Duke Rain Microphysics Column Model** (Prat and Barros, 2007; Wilson and Barros, 2014) simulates interactions not only among raindrops but also between raindrops and fog droplets (Duan and Barros, 2017).

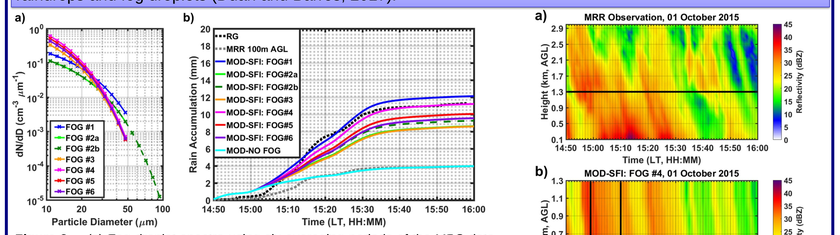

Figure 3 **–** (**a**) Fog droplet spectra using six averaging periods of the MPS data before 14:50; (**b**) Simulated cumulative rainfall with each spectrum used as the fog input in the model, compared to observations from the raingauge (RG) and MRR. "MOD-SFI" indicates model simulations with the presence of fog, thus activating SFI. "MOD-NO FOG" indicates the model simulation without fog.

B. Satellite-based Climatology (10-year: 2006 - 2016) of Low-level clouds and fog (LLCF) using CALIPSO, CloudSat, and MODIS

Cloud Base Height (CBH) using CALIPSO and CloudSat

Figure 4 **–** (**Top**) Mean (**a**) of CALIOP-CPR CBHs (km, AGL) for LLCF (merged CBH < 4 km MSL) and the corresponding coefficient of variance (CV; **b**) in each grid box (0.1° × 0.1°) for daytime overpasses. (**Bottom**) Mean (**c**) of CALIOP CBHs (km, AGL) for LLCF (CALIOP CBH < 4 km MSL) and the corresponding CV (**d**) in each grid box (0.1° × 0.1°) for nighttime overpasses. Contour lines denote terrain elevation of 500 m (solid grey), 1000 m (solid black) and 1500 m (dotted black). Note the three ground ceilometer sites (from left to right: KRHP, KAVL, KGEV) are marked by purple crosses and the numbers next to them represent mean ceilometer CBHs around satellite overpass time.

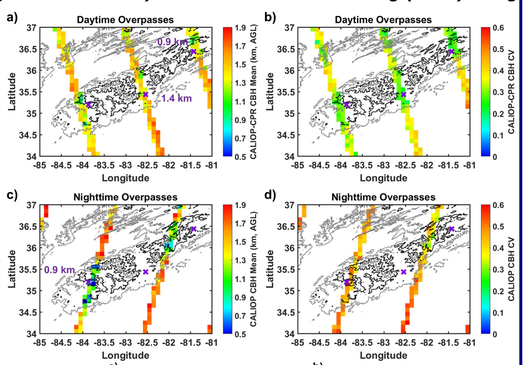

LLCF occurrences using MODIS

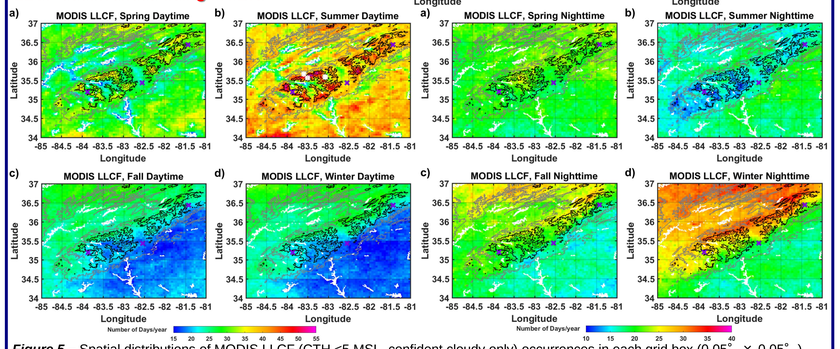

Figure 5 – Spatial distributions of MODIS LLCF (CTH <5 MSL, confident cloudy only) occurrences in each grid box (0.05° × 0.05°) during daytime (Left Column) and nighttime (Right Column) overpasses in each season (spring: April–June; **a**, summer: July–September; **b**, fall: October–December; **c**, and winter: January–March; **d**).

2. Shallow Precipitation Detection and Classification

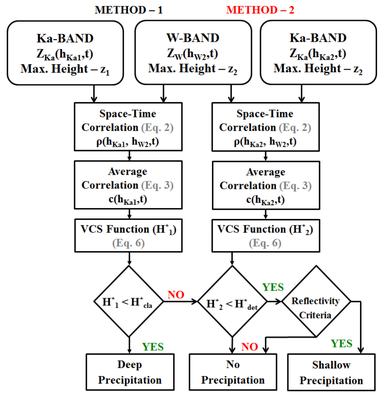

Shallow Rainfall Detection and Classification (SRDC) Algorithm was developed for collocated W-and Ka-Band ground based radar at Maggie Valley, NC during IPHEx to classify low-level and deep precipitation event.

The column and low-level reflectivity profiles of Ka-Band radar and the low-level reflectivity profiles of W-Band are used to compute the column (Method 1) and low-level VCS function (Method 2).

Method-1 and -2 VCS shows variation for clear sky conditions and precipitation structure. Reflectivity profiles with values less than12 dBZ and 0 dBZ for Ka- and W- Band radar respectively are considered as no-precipitation event.

The algorithm was tested on ground-based observations from various locations such as Hyytiala, Finland and Southern Great Plains, Oklahoma.

Figure 5 - *Schematic of Algorithm*

GROUND OBSERVATIONS – IPHEx at Maggie Valley, NC

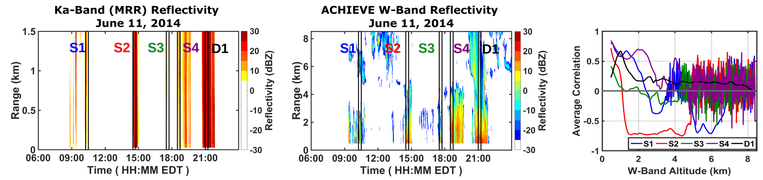

Figure 6 - *Reflectivity profiles observed by collocated (a) MRR and (b) W-Band Radar on June 11, 2014. (c) Average Method-1 space-time correlation of the highlighted events. Note the changes in structure of the average correlation and zero crossing with events.*

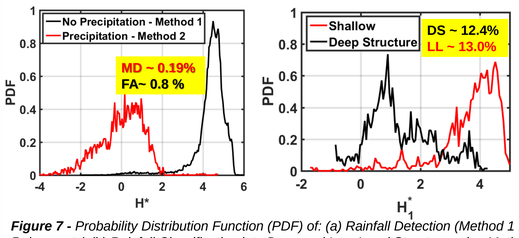

The SRDC algorithm was applied on the collocated W-Band and MRR data at the Maggie Valley, NC during IPHEx-IOP (May 1, 2014 to June 15, 2014). Here, the column profile of W-Band (ACHIEVE) reflectivity is considered to compute Method-1 entropy since the MRR profiles are 1.5 km deep.

Figure 7 - *Probability Distribution Function (PDF) of: (a) Rainfall detection (Method 1 for Non-Rainy Conditions and Method 2 for Rain events) (b) Rainfall Classification into Deep and Low-Level Structure using Method 1 (Column Entropy) and ambiguity error.*

SATELLITE OBSERVATIONS : Concurrent GPM-DPR and CloudSat-CPR observations

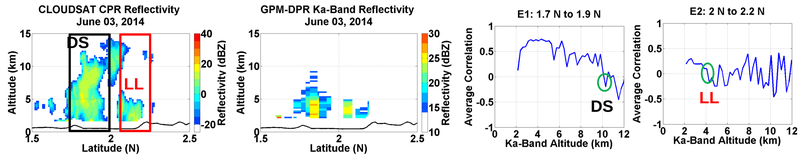

Figure 8 - *Reflectivity profiles observed by concurrent overpasses of (a) CloudSar-CPR and (b) GPM-DPR Ka-Band radar from combined 2BCSATDPR product on June 03, 2014 over Kapuas Mountains in Borneo [115 E]. Two distinct events were highlighted – E1 (black box; deep) and E2 (red box). Average of the space-time correlation between column reflectivity profiles of GPM-DPR (till 12 km) and low-level profiles of CloudSat-CPR (till 4 km) for (c) E1 and (d) E2.* ***The zero-crossing height of the average correlation curve for the deep and shallow precipitation events is marked by the green circle.***

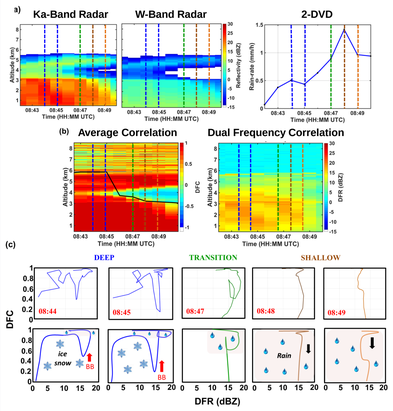

Figure 9 - *(a) Observed Ka- and W-band reflectivity and surface rainfall rate at ARM-TMP on July 14, 2014 including a transition from deep structure to shallow structure rainfall. (b) Dual Frequency Correlation (DFC) and Dual Frequency Ratio (DFR) profiles computed from the observations. (c) Top-row: Temporal evolution of DFC-DFR trajectories at the times marked by the dashed lines of the same color in (a) and (b). Bottom Row: Schematic generalization of evolution of the relationship between DFR and DFC. The blue, green and brown vertical dashed lines in (a) correspond to profiles in the deep structure, transition and shallow structure stages of the events, respectively.*

Note: DFR-DFC relationship from the deep structure stage of the event as the bright-band effect increases and the drop size distribution broadens near the surface (two leftmost panels), through the transition phase without bright-band signature and heavy surface rainfall (central panel), and into the shallow structure stage of event as it weakens and vertical depletion of large drop becomes apparent (two rightmost panels).

3. Evaluation of GPM-DPR using ground observations

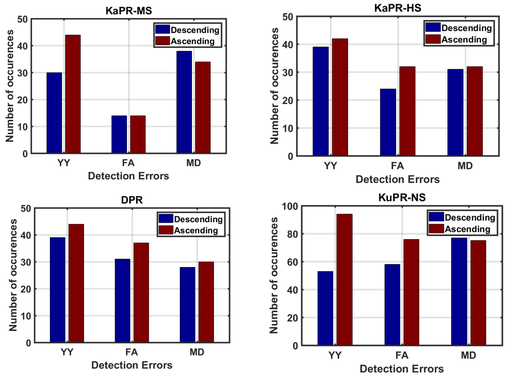

Near-surface precipitation estimates of Level 2, version 5A products of GPM were compared with ground-based rain gauges that lie 2.5 km radius of the DPR pixels.
Time period considered for analysis: March 2014 to May 2017.

Number of correct detections are greater than MD and FA.

Figure 10 **–** *Frequency of correct rainfall detections, False alarms and missed detections of Ka-Band (MS), Ka-Band (HS), DPR and Ku-Band (NS) for ascending and descending scans of GPM-DPR.*

Analysis of Ku-PR Normal scan products:

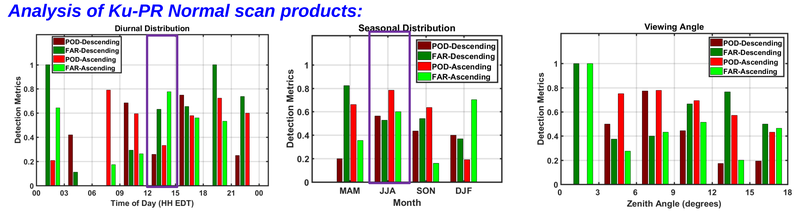

Figure 11 – *GPM Detection Error Analysis: (a) Diurnal Cycle, (b) Seasonal Cycle and (c) Viewing Angle. Note: High FA and MD cases during mid-day, Spring season and off-nadir zenith angle.* POD (or MD) for descending scans shows high variation with zenith angle.

Estimation Errors

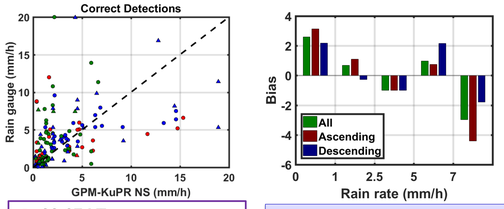

Figure 12 – *GPM Estimation Error Analysis: (a) Scatter plot comparing the precipitation estimates from GPM Ku-Band Precipitation Radar error estimates with Rain gauge observations. (b) Bias between GPM-KuPR and rain rates from rain gauges.*

Late afternoon precipitation (16-23 EDT) are underestimated by GPM-DPR. Ascending scans of morning precipitation show overestimation of rain-rates.

- 00-07 LT
- 08-15 LT
- 16-23 LT
- Ascending
- Descending

RG - Rain rate < 7 mm/h are overestimated
RG - Rain rate > 7mm/h are underestimated.

Case Study – Missed Detection

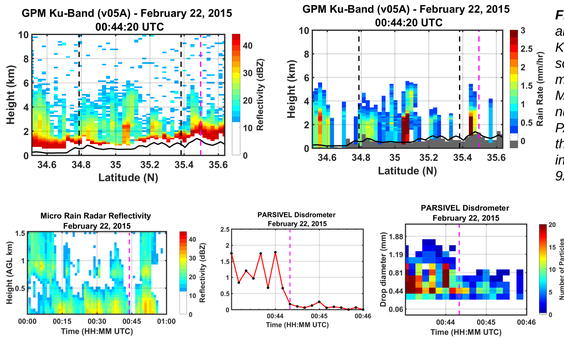

Figure 13 **–** *Top Panel: Reflectivity profiles and Rain-rate profiles estimated by GPM-Ku Band precipitation radar (normal scans). Bottom Panel: Ground-based measurements of reflectivity profiles using Micro Rain Radar, rain-rate and drop number distributions measured by PARSIVEL Disdrometer. Pink lines denote the location of the ground-based instruments (Maggie Valley; elevation – 925 m).*

GPM-Ku Band radar misses the low-level precipitation (with 2 km AGL) due to scan zenith angle and ground-clutter.

5. References and Acknowledgements

Arulraj, M., and Barros, A. P., 2017: Shallow Precipitation Detection and Classification using Multifrequency Radar Observations and Model Simulations, Journal of Atmospheric and Oceanic Technology, 34, 1963–1983, doi:10.1175/JTECH-D-17-0060.1.

Duan, Y. and Barros, A. P., 2017: Understanding how low-level clouds and fog modify the diurnal cycle of orographic precipitation using *in situ* and satellite observations, *Remote Sensing*, *9(9)*, 920; doi:10.3390/rs9090920.

Prat, O. P., and Barros, A. P., 2007: A Robust Numerical Solution of the Stochastic Collection–Breakup Equation for Warm Rain, *Journal of Applied Meteorology and Climatology*, 46, 1480-1497, 10.1175/jam2544.1.

Wilson, A. M., and Barros, A. P., 2014: An Investigation of Warm Rainfall Microphysics in the Southern Appalachians: Orographic Enhancement via Low-Level Seeder–Feeder Interactions, *Journal of the Atmospheric Sciences*, *71*(5), 1783-1805, doi:10.1175/jas-d-13-0228.1.

–Acknowledgments: This research is supported by the NASA PMM program.